Proceedings of the Conference on Computational Engineering and Science JSCES
Vol. 30, Jun. 2025

Topology optimization for multi-axis additive subtractive manufacturing with curved layer generation

Shuzhi Xu[1] and Kentaro Yaji[2]

1) Ph.D. The University of Osaka, Specially Appointed Researcher（2-1, Yamadaoka, Suita, Osaka, E-mail: xu@syd.mech.eng.osaka-u.ac.jp）

2) Ph.D. The University of Osaka, Associate Professor（2-1, Yamadaoka, Suita, Osaka, E-mail: yaji@syd.mech.eng.osaka-u.ac.jp）

This paper presents a concurrent structure and process topology optimization method, aiming to simultaneously design the structure, slicing strategy, and manufacturing sequences for multi-axis hybrid additive and subtractive manufacturing. A novel approach based on the heat diffusion equation and Poisson equation is proposed to generate curved slicing layers, while ensuring that all slicing-related information is fully derivable. In addition, sequence division thresholds are optimized to determine when to alternate between additive manufacturing and subtractive machining operations. To realize concurrent optimization and ensure manufacturability, a coupled and differentiable optimization model is established. This includes a self-support constraint to eliminate the need for support structures, and a curvature constraint to maintain uniform layer thickness. Moreover, a collision-free constraint—integrated with the planned sequences—is introduced to prevent tool collisions during the subtractive process. To validate the effectiveness of the proposed method, a representative 3D numerical example is investigated.

Key Words : *Topology optimization, design for manufacturing, hybrid additive subtractive manufacturing*

1. INTRODUCTION

In the fields of aerospace, energy engineering, and biomedical applications, optimizing complex structures is crucial for enhancing product performance. The design of heat exchangers, hydraulic components, and high-performance lightweight structures require optimized material distribution under complex operating conditions. This optimization ensures that multiple performance requirements, such as strength, stiffness, and flow resistance, are met simultaneously. However, traditional design methods primarily rely on experience or parameter tuning based on extensive experimental trials, making it challenging to achieve truly optimal designs under complex constraints.

In recent years, topology optimization has emerged as a powerful computational design method capable of automatically generating optimized material distributions and complex geometries through mathematical optimization under given functional requirements and physical constraints [1]. As a mathematically driven and simulation-based optimization approach, topology optimization surpasses the limitations of traditional experience-driven design, enabling more efficient, lightweight, and innovative engineering designs. Despite its significant advantages in improving structural performance, existing topology optimization methods are primarily focused on idealized manufacturing environments and often do not fully account for fabrication constraints [2]. As a result, optimized structures frequently exhibit highly complex freeform geometries, such as overhang geometry features and intricate internal channels, which are challenging to fabricate directly using traditional Subtractive Manufacturing (SM) or Additive Manufacturing (AM) techniques. This limitation obstructs the practical implementation of topology-optimized designs in real-world engineering applications.

Hybrid Additive-Subtractive Manufacturing (HASM) offers a new approach to addressing this challenge [3]. HASM integrates high-efficiency AM such as DED, with high-precision SM such as milling and grinding within a single manufacturing system (Fig.1), Technology allows direct control over part dimensions during fabrication, improving geometric accuracy and surface quality while mitigating defects commonly associated with standalone AM. Compared to conventional SM, HASM enables localized finishing, enhances machining efficiency, and facilitates one-step fabrication of complex structures, making topology-optimized designs more viable for real-world applications.

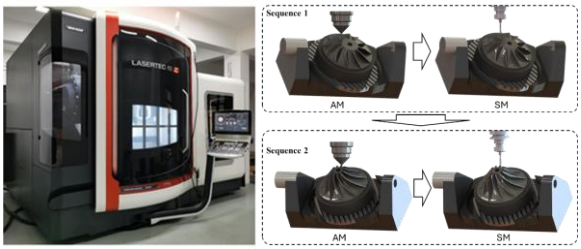

Fig. 1 The DMG LASERTEC 65 3D Hybrid integrates an additive manufacturing system in the conventional CNC machine center.

However, existing topology optimization methods have not yet been adapted for HASM [4]. Since the HASM process involves dynamic material addition, removal, and reprocessing, conventional topology optimization approaches struggle to effectively coordinate the feasibility of HASM. This limitation may lead to designs that are manufacturable in the additive phase but difficult to process in the subtractive stage. Additionally, current topology optimization primarily focuses on material distribution while neglecting essential process parameters such as toolpath and operation sequence planning. In HASM, machining paths and process parameters (e.g., tool feed direction, cutting depth, and layer thickness control) directly influence manufacturing precision, mechanical performance, and surface quality. Therefore, topology optimization must not only optimize structural topology but also

adaptively refine HASM process parameters to ensure both manufacturability and efficiency. This necessitates a deeper integration of topology optimization with advanced manufacturing technologies. Only by establishing a comprehensive topology optimization framework that fully incorporates the capabilities of HASM can we achieve an efficient transition from theoretical designs to manufacturing structures.

So, in this work, we proposed an optimization framework that simultaneously designs the structure, slices, and sequences for multi-axis hybrid additive and subtractive manufacturing.

2. Problem definition

For the HASM, the issues underlying structure optimization and process optimization, which can be categorized into two parts: additive and subtractive processes.

In the additive process, the slicing quality determines the success rate of printing. We primarily consider the following two aspects: 1) The angle between the normal vector of each slice and the density gradient should exceed a threshold, typically 45 degrees, to achieve the structure self-support (Fig.2). 2) The slice thickness should remain uniform during the multi-axis AM. Significant variations in thickness pose challenges in controlling the material deposition rate to ensure satisfactory printing quality.

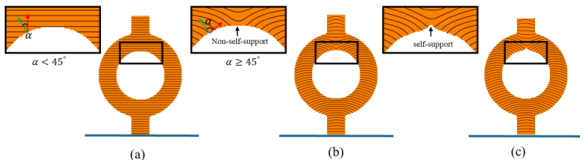

Fig. 2 The typical self-support issue happened in AM: (a) the overhang geometry feature on the top of the ring which might induce some printing difficulty in planer-based AM; (b) if just optimizing the path, such kind issue will still exist even using multi-axis AM; (c) concurrent optimization of the structure and path will totally solve this issue.

Regarding the subtractive process, the entire structure surface should be accessible for machining. If only a single additive-subtractive (AM-SM) sequence is used, collisions may occur due to excessively deep slots and limited tool length. However, by implementing multiple AM-SM sequences, this issue can be mitigated by reducing the cutting depths at each stage. Therefore, determining the optimal timing for switching between additive and subtractive operations is a critical challenge in optimizing the HASM workflow.

3. Additive manufacturing geometry constraint

(1) The derivable printing path achievement

In this work, the AM constraints are implemented based on the corresponding slicing paths. We employ the geodesic in heat method [5] to achieve this. Firstly, a heat source assigned to the print platform diffuses heat throughout the entire structure:

$$\begin{cases} \nabla \cdot (\kappa \nabla T) = 0 \\ T = T_{\text{start}} \ \text{on} \ \Gamma_{\text{start}} \\ T = T_{\text{end}} \ \text{on} \ \Gamma_{\text{end}} \\ \nabla T \cdot \mathbf{n} = 0 \ \ \text{on} \ \Gamma \setminus (\Gamma_{\text{end}} \cup \Gamma_{\text{start}}) \end{cases}, \tag{1}$$

where ∇ is the differential operator, and $\mathbf{n}$ is the outward normal vector of the boundary, Γ indicates for the boundary of the domain. This Partial Differential Equation (PDE) represents steady-state heat conduction within a heterogeneous medium, featuring with varying thermal diffusivity κ. Γ_{start} indicates the boundary where the printing starts, and Γ_{end} indicates the boundary where the printing ends. However, the temperature field T just indicates a poor approximation of the geodesic distance due to its high sensitivity to the distance from the heat source (as shown in Fig.1(b)). Therefore, instead of directly using the field T, it is needed to build a replacement scalar field, also denoted as $\boldsymbol{\varphi}$, which possesses similar properties to the field T and very importantly, uniform gradient norms (as shown in Fig.1(c)). Then, the corresponding spatial and temporal information for AM can be obtained from this scalar field $\boldsymbol{\varphi}$. To achieve a satisfactory $\boldsymbol{\varphi}$, we begin by normalizing the temperature gradients to achieve a unit temperature gradient $\boldsymbol{\omega} = \frac{\nabla T}{\|\nabla T\|}$, and then, forcing the scalar field $\boldsymbol{\varphi}$ to approach the following condition:

$$\nabla \varphi = \boldsymbol{\omega}, \quad \varphi = T_{\text{start}} \ \text{on} \ \Gamma_{\text{start}}, \tag{4}$$

The main purpose of making $\varphi = T_{\text{start}}$ on Γ_{start} is to ensure the initial printing direction consistency between φ and T, while enforcing $\nabla \varphi = \boldsymbol{\omega}$ is to guarantee the printing orientation consistency between φ and T. Typically, the scalar field φ can be obtained by solving the following optimization model:

$$\begin{cases} \text{find: } \varphi \\ \text{minimize: } \mathrm{F} = \int (\nabla \varphi - \boldsymbol{\omega})^2 \mathrm{d}\Omega_{\mathrm{D}}, \\ \varphi = \mathrm{T}_{\text{start}} \ \text{on} \ \Gamma_{\text{start}} \end{cases} \tag{3}$$

Alternatively, we can solve the problem in Eq.(7) using variational theory. This means that Eq.(7) can be transformed into solving the following equation:

$$\begin{cases} \Delta \varphi = \nabla \cdot \boldsymbol{\omega} \\ \varphi = T_{\text{start}} \ \text{on} \ \Gamma_{\text{start}} \end{cases}, \tag{4}$$

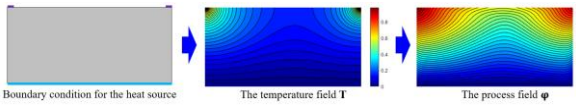

Fig. 3 The procedure of the process field realization: (a) the boundary condition for the geodesic in heat method; (b) the temperature distribution; (c) the process field distribution, and the isoline is the real printing layer.

The process described in this subsection is illustrated in Fig.3. Based on the obtained process field $\boldsymbol{\varphi}$, we can explicitly represent the machining path by extracting its contour lines. Additionally, the process field defines the minimum machining unit, forming the fundamental basis for all subsequent machining constraints.

(2) The self-support constraint

Based on the obtained process field, the first geometry constraint is the self-support constraint, which is achieved by controlling the difference between the gradient direction of the structural field $\mathbf{g} = \left(\frac{\partial \rho}{\partial x}, \frac{\partial \rho}{\partial y}\right)$ and the gradient direction of the process field $\mathbf{b} = \left(\frac{\partial \varphi}{\partial x}, \frac{\partial \varphi}{\partial y}\right)$:

$$\chi = \mathbf{b} \cdot \mathbf{g} - \|\mathbf{b}\| \cdot \|\mathbf{g}\| \cdot \cos \theta_0, \tag{5}$$

χ represents the magnitude of the difference between the two in each element. The overhang surface is defined as the boundary where all the overhang angle θ is larger than a specific value θ_0. Then, the field χ will be further projected into a 0-1 binary vector through Heaviside projection, which is subsequently used to construct a volume fraction constraint:

$$\Psi_{\text{sup}} = \frac{1}{\text{N}} \sum_{e \in \Omega_{\text{D}}} \frac{\chi_e}{1 + \text{e}^{-\beta \chi_e}} \leq \text{V}_{\text{tol}}, \tag{6}$$

where β is still the sharpness control parameter. The primary purpose of Eq.(6) is to minimize the number of boundary elements that fail to satisfy the self-support condition, thereby achieving the self-support effect of the overall structure. To avoid potential numerical issues, V_{tol} needs to be a very small value (but still greater than 0).

(3) The slice curvature constraint

The second one is the curvature constraint, in two-dimensional space, the divergence of the layer normal vector equals its curvature. In three-dimensional space, the divergence of the normal vector of the curved layer corresponds to its principal curvature of the surface. This relationship allows us to establish a constraint on the curvatures of the slices. The calculation of divergence is performed as follows:

$$\psi = \nabla^2 \varphi \tag{7}$$

Where ∇^2 means the Laplacian operation, then ψ is defined to quantify the local curvature in a neighborhood surrounding the element e:

$$\bar{\psi}_e = \frac{\sum_{i \in \Omega_e} \psi_i}{\sum_{i \in \Omega_e} 1} \tag{8}$$

where Ω_e is the set of all surrounding elements with centroids falling inside a given radius R, i.e.

$$\Omega_e = \{i | \, \|x_i - x_e\|_2 \leq R\} \tag{9}$$

x_i and x_e are the centroids of the elements. R is set to 5 in this work. The positions and lengths are measured in units of voxels. Finally, the constraint on curvature is also established as a global p-norm constraint [6]:

$$\Psi_{\text{cur}} = \left(\frac{1}{\text{N}} \sum\nolimits_{e=1}^{\text{N}} \left(\sqrt{\bar{\psi}_e^2} \right)^p \right)^{\frac{1}{p}} \leq \overline{\omega} \tag{10}$$

where $\overline{\omega}$ is a maximum curvature threshold. p is the p-norm parameter, chosen as 16 in this work.

4. Subtractive manufacturing geometry constraint

The subtractive constraints are primarily reflected in the multi-axis subtractive tool accessibility constraints. To prevent collisions during the subtractive process, and make sure all the surfaces could be successfully milling. The convolution method is utilized for cutting tool collision detection:

$$\boldsymbol{\xi}_i = \text{conv}(\bar{\boldsymbol{\rho}}, \mathbf{R}_i), \tag{11}$$

$\boldsymbol{\xi}_i$ represents the inaccessible areas under the i^{th} tool feed direction, or in other words, the collision-encountered tool tip areas during machining. $\mathbf{R}_i$ is the binary convolution kernel, which mimics the shape of the cutting tool. conv(), represents the convolution operator. The detailed detection process can be found in [7]. If multiple feed directions exist, the p-norm function is applied to combine the inaccessible domains corresponding to each feed:

$$\bar{\boldsymbol{\xi}} = \left(\frac{1}{I} \sum\nolimits_{i=1}^{I} (\boldsymbol{\xi}_i)^q \right)^{\frac{1}{q}}, \tag{12}$$

I represents the total number of feeds. Taking q as a negative value (set to be -4 here) allows extracting the approximate minimum value from each $\boldsymbol{\xi}_i$. For convenience in subsequent expressions, we unify the process described in Equations (11) and (12) as:

$$\bar{\boldsymbol{\xi}} = \text{sm}(\bar{\boldsymbol{\rho}}, \mathbf{R}) \tag{13}$$

5. Hybrid additive subtractive manufacturing

As mentioned in the introduction, the advantage of HASM lies in its capability to finish complex structures through the alternating processes of additive and subtractive. This section will focus on optimizing the process planning of these additive and subtractive alterations to fully leverage their benefits.

The additive process is organized into layers based on the process field $\boldsymbol{\phi}$. Therefore, the planning of the additive-subtractive sequences should align with the sliced layers. In other words, sequence planning should also be conducted on top of the process field. The process field can be divided into several segments, each representing an alternating sequence by assigning a scalar indicator through projection.

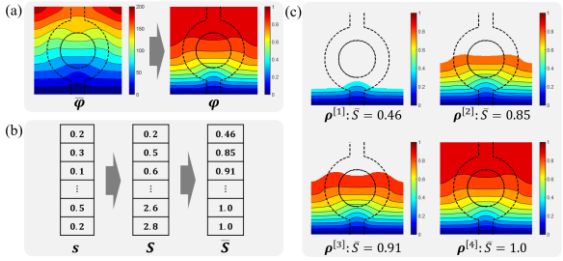

Fig. 4 The illustration of sequence planning within this work: (a) the process field before and after normalization; (b) the illustration of the sequence control variable; (c) the corresponding fabricated structure in different sequence.

A set of ascendingly ordered scalars are needed to divide the manufacturing process into sequences. To create this ordered set, a column of sequence division variables is introduced, denoted as $\boldsymbol{s}$. These variables are arranged sequentially between 0 and 1 as follows:

$$\boldsymbol{s} = \{s_1, s_1, \ldots, s_m\}, \qquad 0 < s_1, s_1, \ldots, s_M < 1, \tag{14}$$

Here, m represents the sequence index, and M is the total number of sequences. Subsequently, by performing cumulative summation, we obtain:

$$\boldsymbol{S} = \text{cumsum}(\boldsymbol{s}), \tag{15}$$

In this work, we consider only the values of $\boldsymbol{s}$ between 0 and 1 as valid local process steps. For values of $\boldsymbol{s}$ greater than 1, they are equivalent to covering the entire geometry. To achieve this, we apply the sigmoid function to normalize $\boldsymbol{s}$:

$$\bar{\boldsymbol{S}} = \frac{2}{1 + e^{-\beta_s \boldsymbol{S}}} - 1, \tag{16}$$

Based on the aforementioned function, we can ensure that for values between 0 and 1, $\bar{\boldsymbol{S}}$ remains consistent with $\boldsymbol{S}$, while for values of $\boldsymbol{S}$ greater than 1, $\bar{\boldsymbol{S}}$ consistently takes the value of 1. β_s is the sharpness parameters for sigmoid function, in here, taking the value as 4. We also need to normalize the process field. Here, we similarly use the sigmoid function:

$$\bar{\boldsymbol{\varphi}} = \frac{2}{1 + e^{-\beta_\varphi \boldsymbol{\varphi}}} - 1, \tag{17}$$

β_φ will take 10 in here to achieve a numerical stability. Then, the normalized process field $\bar{\boldsymbol{\varphi}}$ can be divided into multiple sequences using the smoothed Heaviside function.

$$\tau_e^{[m]} = \frac{\tanh(\beta_t \bar{S}_m) + \tanh(\beta_t (\bar{\varphi}_e - \bar{S}_m))}{\tanh(\beta_t \bar{S}_m) + \tanh(\beta_t (1 - \bar{S}_m))}, \tag{18}$$

So, the structure after the additive process in the m^{th} sequence is:

$$\rho_e^{[m]} = \bar{\tilde{\rho}}_e \tau_e^{[m]}. \tag{19}$$

The collision region for the m^{th} sequence can be calculated using the following equation:

$$\begin{aligned}\boldsymbol{\psi}^{[1]} &= \mathrm{sm}(\boldsymbol{\rho}^{[m]}, \mathbf{R}) \circ (1-\boldsymbol{\rho}^{[m]}) \\ \boldsymbol{\psi}^{[m]} &= \mathrm{sm}\left(\boldsymbol{\rho}^{[m]}, \mathbf{R}\right) \circ \left(\boldsymbol{\tau}^{[m]} - \boldsymbol{t}^{[m-1]}\right) \circ (1-\boldsymbol{\rho}^{[m]}) \\ &, m = 2, 3, \dots, M.\end{aligned} \tag{20}$$

where $\circ$ represent the Hadamard product. Ultimately, the total number of detected collisions serves as the cutting tool collision constraint:

$$\Psi_{\mathrm{col}} = \frac{1}{N}\sum_{m=1}^{M} \boldsymbol{\psi}^{[m]} \leq \delta. \tag{21}$$

δ represents a small value which could avoid singularity.

6. Optimization model and its numerical implementation

The proposed concurrent optimization model for HASM involves three components: the density variable optimization, the process variable optimization, and the sequence optimization. These components will work together to represent the structure and manufacturing information. The optimization model is decomposed into three sub-models to clarify the relationship between the variables, constraints, and the objective function. The specific expression of the model is as follows, first for the design variable updating:

$$\begin{cases} find: \rho \\ min: \ c(\rho) \\ st. \begin{cases} V(\rho) \leq V_0 \\ \Psi_{\mathrm{sup}} \leq \mathrm{V_{tol}} \\ \Psi_{\mathrm{col}} \leq \overline{\omega} \\ 0 \leq \rho_e \leq 1 \end{cases} \end{cases}. \tag{22}$$

where $c()$ represents the performance of the structure. In this work, we consider thermal compliance [8]. V represent the volume fraction, and V_0 is the predefined volume fraction limit. Next is the optimization model regarding the auxiliary domain process field:

$$\begin{cases} find: \varphi \\ min: \ \Psi_{\mathrm{sup}} \\ st. \begin{cases} \Psi_{\mathrm{cur}} \leq \overline{\omega} \\ 0 \leq \ \varphi_e \leq 1 \end{cases} \end{cases}. \tag{23}$$

The main purpose of optimizing the process field is to relieve the constraint violation of self-support in sub-model I and to ensure the quality of the slices for successful printing. So that, this model defines the objective function as the self-support function, and two additional constraints related to layer generation are introduced. Lastly, the optimization model concerning the sequence variables is given:

$$\begin{cases} find: s \\ min: \ \Psi_{\mathrm{col}} + \Psi_{\mathrm{cost}} \\ st. \quad 0 \leq s_m \leq 1 \end{cases}. \tag{24}$$

In this model, the manufacturing cost is established. Generally, the more frequently the additive and subtractive processes are interlaced, the higher the time cost for manufacturing is consumed. To minimize the number of changes between additive and subtractive operations, the following cost equation is proposed:

$$\Psi_{\mathrm{cost}} = \sum_{m}^{M} 1 - \bar{S}_m. \tag{25}$$

To minimize the value in the cost equation above, all sequence variables should approach 1. This indicates maximizing the additive process until a collision occurs, which reduces the number of alternations.

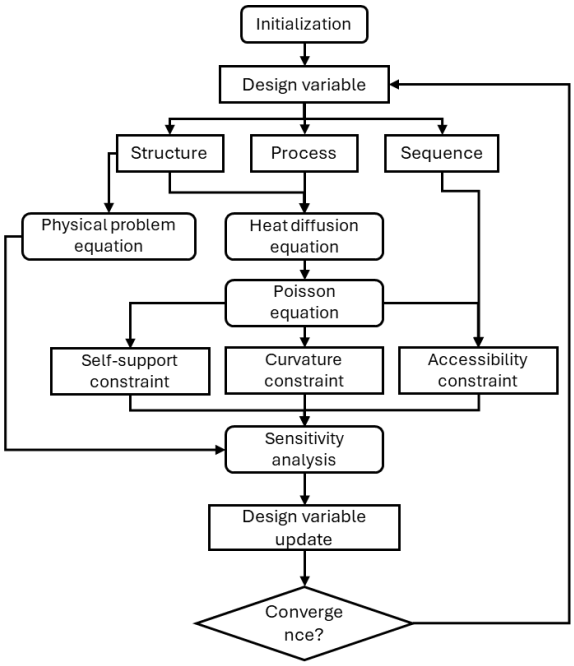

Fig. 5 The flowchart of proposed method

Fig.5 illustrates the flowchart of the proposed algorithm framework, which consists of the following four main steps:

Step 1: Initialize all relevant parameters along with the three design variables.

Step 2: The density field is utilized to solve physical problems, such as heat conduction. Simultaneously, it is coupled with the process control field to construct the heat diffusion equation. Solving this equation yields the temperature field, which is then used to compute the process scalar field and the normal vectors of the slicing planes via the Poisson equation. These normal determine the orientation of the printing platform.

Step 3: Manufacturing quality constraints—including the self-support constraint and the curvature constraint—are imposed on the slices. Meanwhile, the scalar field derived from the Poisson equation is segmented into multiple sequences based on predefined division thresholds, thereby establishing a collision-free constraint for the cutting tool.

Step 4: Sensitivity analysis is conducted on the objective function and the imposed constraints. The design variables are then updated using the Method of Moving Asymptotes (MMA) [9]. If convergence is achieved, the final output is generated; otherwise, Steps 2 to 4 are repeated iteratively.

7. Numerical results

In this section, a 3D heat conduction problem is investigated to show the effectiveness of the proposed method. The boundary conditions are shown in Fig.6, which divides the entire design space into cubic units measuring $96 \times 96 \times 80$. Homogeneous Dirichlet boundary conditions are applied to the central eight units at the bottom. To save computational resources, only one-quarter of the design space, which is symmetrical, is considered for calculations. The maximum volume proportion is set at 12%. The curvature threshold $\overline{\omega}$ is set to 0.1.

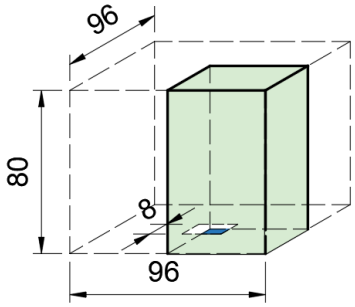

Fig. 6 Design domain and boundary conditions for heat sink in 3D

Fig.7 illustrates the optimization results, the optimized structure is shown in Fig.7 (a), and the corresponding multi-axis AM slices, and the sequence planning results are shown in Fig.7 (b). Different colors represent different machining sequences. After optimization, a total of four sequences remains. Most importantly, each sequence is defined based on the corresponding slicing results.

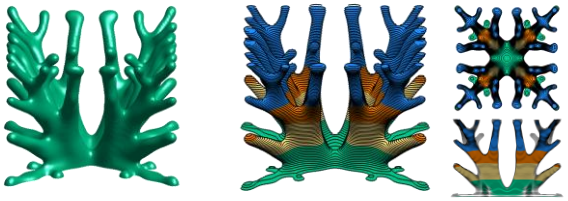

(a) (b)

Fig. 7 (a) the optimized structure; (b) the curved slices and its corresponding sequence planning results (different color indicates different sequence, and there are totally 4 steps involved in this result)

Fig. 8 shows the convergence curves of the entire optimization process. Three representative metrics are plotted: the objective function (thermal compliance), the area of non-self-supporting regions, and the area of inaccessible regions. As observed, the objective function decreases gradually and eventually stabilizes as optimization progresses. Meanwhile, both constraints are effectively satisfied and remain stable in the later stages of the optimization. This demonstrates that the optimization process has successfully converged.

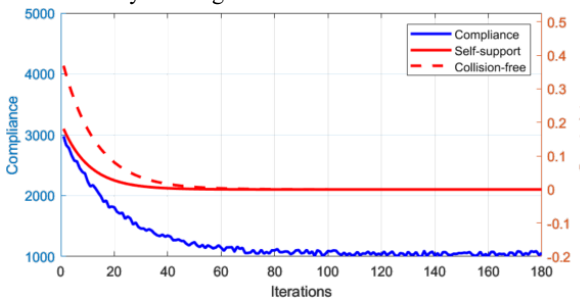

Fig. 8 The convergence history

Subsequently, in Fig.9, we present a detailed illustration of the alternating additive-subtractive manufacturing process, along with its effects on the structural surface.

Fig.10 illustrates the optimization results under various design methods. As observed on Fig.10, the heat sink performs best ($c = 983.8$) without any manufacturing constraints. In comparison, the increase in thermal compliance is only 5.6% ($c = 1014.1$) for the five-axis self-support design. Additionally, when the collision-free constraint is introduced, the structure's thermal compliance adds by 12.2% ($c = 1052.2$). This proposed result ensures fabrication feasibility while minimizing the sacrifice of structural efficiency.

(a) (b) (c)

Fig. 10 The comparison of the results with different design method: (a) the conventional topology optimization result (no manufacturing constraint) [10]; (b) the 5-axis AM oriented result with curved slice (self-support constraint is considered) [11]; (c) the proposed HASM oriented result with curved slice and sequence planning.

8. Conclusion

In this work, we addressed the challenge of concurrently optimizing structural design and manufacturing process in the context of multi-axis HASM. A concurrent topology optimization model was developed, integrating a series of complex manufacturability constraints. Notably, the proposed model is capable of simultaneously generating an optimized structural layout, curved slicing paths for additive manufacturing, and a detailed process plan for alternating AM-SM operations. The method was validated through a representative 3D numerical example, and the following conclusions can be drawn.

Nevertheless, there remain several aspects for future improvement. One key limitation is the lack of experimental validation. Although the proposed framework provides detailed slicing data and a comprehensive AM-SM process plan, its practical feasibility has not yet been tested experimentally. To proceed with physical validation, stable melt pool control must be ensured. Issues such as part distortion and insufficient deposition height—both of which are strongly influenced by melt pool dynamics—pose significant challenges that can disrupt the actual manufacturing process.

ACKNOWLEDGMENT: This work was supported by JSPS KAKENHI (Grant No. 23H03799).

Besides, the authors would like to thank Dr. Yifan Guo from University of Alberta, Canada for his help in presenting the results.

REFERENCES

[1] Bendsoe, M. P., & Sigmund, O. (2013). *Topology optimization: theory, methods, and applications*. Springer Science & Business Media.

[2] Liu, J., Gaynor, A. T., Chen, S., Kang, Z., Suresh, K., Takezawa, A., ... & To, A. (2018). Current and future trends in topology optimization for additive manufacturing. *Structural and multidisciplinary optimization*, *57*(6), 2457-2483.

[3] Grzesik, W. (2018). Hybrid additive and subtractive manufacturing processes and systems: A review. *Journal of Machine Engineering*, *18*(4), 5-24.

[4] Liu, J., Huang, J., Zheng, Y., Hou, S., Xu, S., Ma, Y., ... & Li, L. (2023). Challenges in topology optimization for

hybrid additive–subtractive manufacturing: A review. *Computer-Aided Design*, *161*, 103531.

[5] Crane, K., Weischedel, C., & Wardetzky, M. (2013). Geodesics in heat: A new approach to computing distance based on heat flow. *ACM Transactions on Graphics (TOG)*, *32*(5), 1-11.

[6] Wu, J., Aage, N., Westermann, R., & Sigmund, O. (2017). Infill optimization for additive manufacturing—approaching bone-like porous structures. *IEEE transactions on visualization and computer graphics*, *24*(2), 1127-1140.

[7] Xu, S., Liu, J., Yaji, K., & Lu, L. (2024). Topology optimization for hybrid additive-subtractive manufacturing incorporating dynamic process planning. *Computer Methods in Applied Mechanics and Engineering*, *431*, 117270.

[8] Andreassen, E., Clausen, A., Schevenels, M., Lazarov, B. S., & Sigmund, O. (2011). Efficient topology optimization in MATLAB using 88 lines of code. *Structural and Multidisciplinary Optimization*, *43*, 1-16.

[9] Svanberg, K. (1987). The method of moving asymptotes—a new method for structural optimization. *International journal for numerical methods in engineering*, *24*(2), 359-373.

[10] Liu, K., & Tovar, A. (2014). An efficient 3D topology optimization code written in Matlab. *Structural and multidisciplinary optimization*, *50*(6), 1175-1196.

[11] Xu, S., Liu, J., He, D., Tang, K., & Yaji, K. (2025). Self-support structure topology optimization for multi-axis additive manufacturing incorporated with curved layer slicing. *Computer Methods in Applied Mechanics and Engineering*, *438*, 117841.

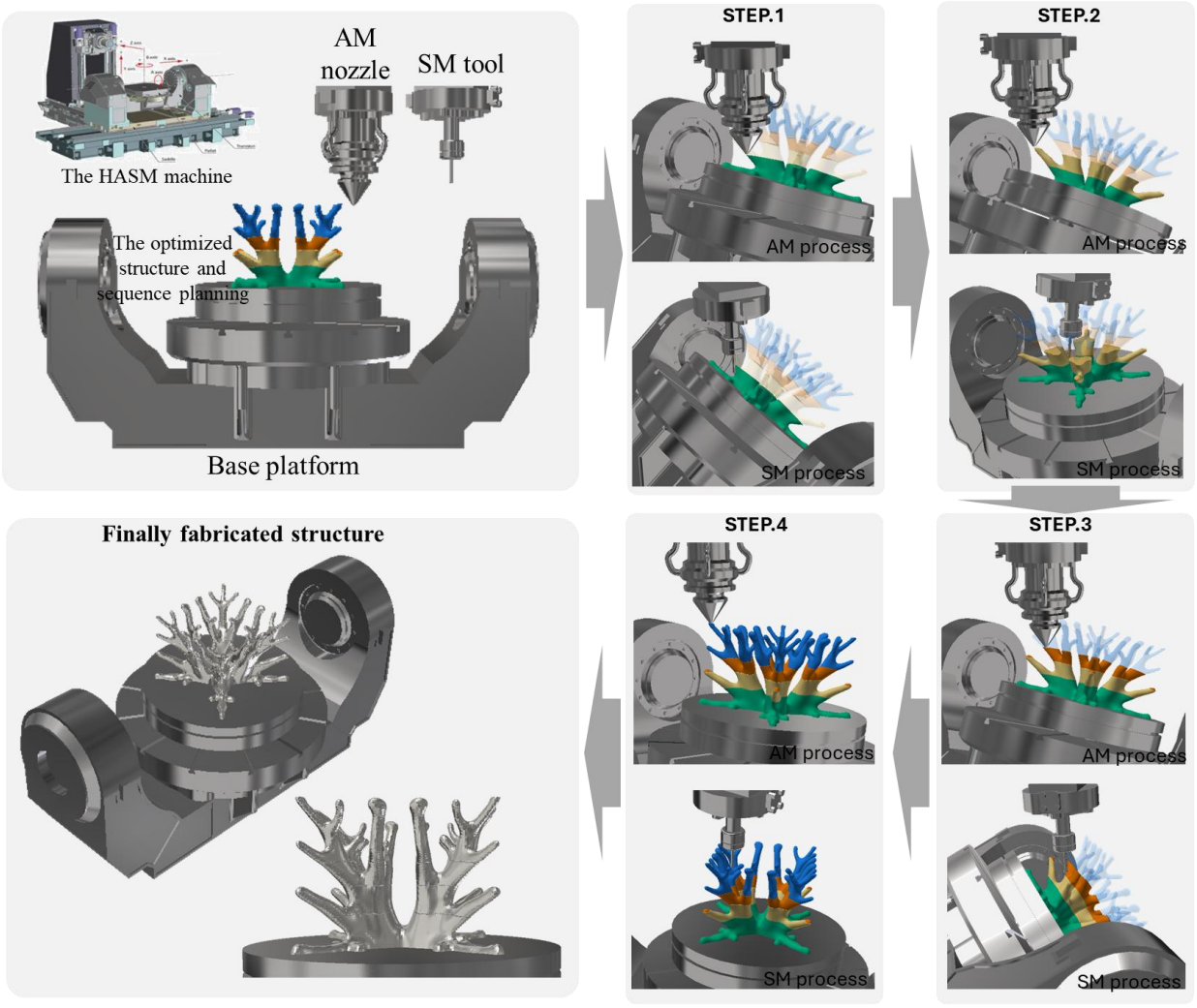

Fig. 9 The illustrations for the structure and fabrication sequence optimized by proposed method using HASM.